

Noise in supercontinuum generated utilizing PM and non-PM tellurite-glass all-normal dispersion fibers

SHREESHA RAO D. S.^{1,*}, TANVI KARPATE², AMAR NATH GHOSH^{3,4}, IVÁN B. GONZALO¹, MARIUSZ KLIMCZAK², DARIUSZ PYSZ⁵, RYSZARD BUCZYŃSKI^{2,5}, CYRIL BILLET³, OLE BANG^{1,6}, JOHN M. DUDLEY³, AND THIBAUT SYLVESTRE³

¹DTU Fotonik, Department of Photonics Engineering, Technical University of Denmark, Ørsteds Plads, 2800 Kongens Lyngby, Denmark

²University of Warsaw, Faculty of Physics, Pasteura 7, 02-093 Warsaw, Poland

³Institut FEMTO-ST, CNRS, UMR 6174, Université Bourgogne Franche-Comté, Besançon, France

⁴Optoelectronics Research Centre, University of Southampton, Southampton, SO17 1BJ, United Kingdom

⁵Łukasiewicz Research Network - Institute of Microelectronics and Photonics, Al. Lotników 32/46, Warsaw, 02-668, Poland

⁶NKT Photonics A/S, Blokken 84, 3460 Birkerød, Denmark

*Corresponding author: shreesharaods@gmail.com

Compiled February 12, 2022

Intensity fluctuations in supercontinuum generation are studied in polarization-maintaining (PM) and non-PM all-normal dispersion tellurite photonic crystal fibers. Dispersive Fourier transformation was used to resolve shot-to-shot spectra generated using 225 fs pump pulses at 1.55 μm , with experimental results well-reproduced by vector and scalar numerical simulations. By comparing the relative intensity noise (RIN) for the PM and non-PM cases, supported by simulations, we demonstrate the advantage of the polarization maintaining property of the PM fibers in preserving low-noise dynamics. We associate the low-noise in the PM case with the suppression of polarization modulation instability. © 2022 The Authors

<http://dx.doi.org/10.1364/OL.XX.XXXXXX>

Motivated by important applications that require low-noise broadband light sources, there has been much recent interest in supercontinuum (SC) generation in all-normal dispersion (ANDi) fiber [1–4]. In addition to providing a flat-top and broadband spectrum, SC generated in ANDi fibers yields high shot-to-shot coherence due to the relative insensitivity to input noise of self-phase modulation and optical wave breaking dynamics in the normal dispersion regime. The superior noise properties of ANDi SC over SC generated by pumping in the anomalous dispersion have been verified by measurements of spectral coherence using unequal path Michelson interferometers, RF beating with stabilized laser diodes, relative intensity noise (RIN), and dispersive Fourier transformation (DFT) spectral fluctuations [5–8]. However, it has also been established that SC coherence in ANDi fibers can degrade with increased pulse duration and fiber length due to parametric interaction between coherent and incoherent components [9], as well as polarization modulation instability (PMI) [10].

Experiments have used both polarization maintaining (PM)

and weakly birefringent (non-PM) ANDi fibers to demonstrate low-noise SC generation. With PM-ANDi fiber, low-noise SC can be obtained by matching the linear pump polarization to one of the principal axes of the fiber [8, 11, 12]. With non-PM-ANDi fiber, the onset of PMI depends on the pump pulse duration (T_0), fiber length, and peak power (P_0) [10]. As a result, very specific pump parameters and fiber lengths need to be chosen to avoid PMI induced noise, limiting the spectral broadening that can be achieved [7].

A difficulty with these previous studies, however, is that the range of experimental parameters used make it difficult to quantitatively compare the SC properties obtained using PM and non-PM ANDi fiber. In this Letter, we address this problem directly through a combined experimental and numerical study of SC noise in PM and non-PM ANDi fibers under controlled conditions. Specifically, we use two variants of a highly nonlinear tellurite glass photonic crystal fiber (PCF) with all-normal dispersion; one fabricated with polarization-maintaining functionality, the other without. Both variants share a hexagonal air-hole lattice structure. The DFT technique is used to quantify the RIN of SC generated in both fibers, and we explicitly show the superior noise properties of the PM-ANDi fiber variant. These experimental results are supported by numerical simulations using both scalar and coupled vector generalized nonlinear Schrödinger equation (GNLSE) models.

The non-PM fiber (labelled NL47A4), was previously studied for its SC performance in Ref. [13]. This fiber was used as the starting point to develop a PM variant, (labelled NL51A3.2). Scanning electron microscope (SEM) images of both fibers are shown in Fig. 1(a,b). The measured group velocity dispersion (GVD) of the non-PM and the two degenerate modes of the PM fiber is plotted on the left axis of Fig. 1(c). The right axis of Fig. 1(c) plots the measured group birefringence of the PM fiber.

Pulses with full width half maximum, $T_{FWHM} = 225$ fs from an optical parametric oscillator (Coherent Chameleon compact) at 1.55 μm and a repetition rate of 80.15 MHz were used to generate SC in both fibers. A 40 \times microscope objective was

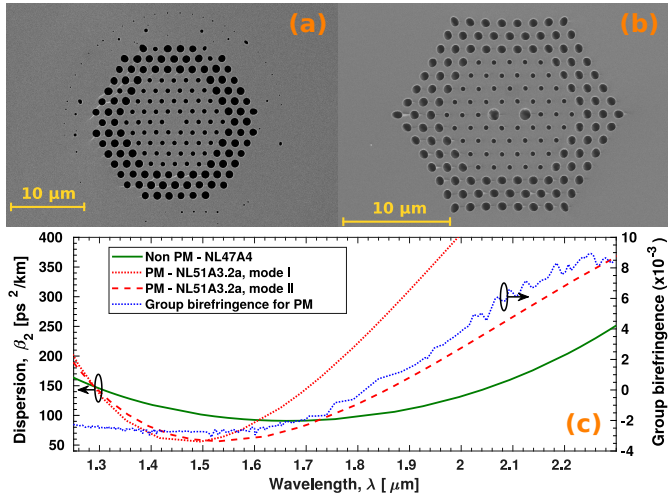


Fig. 1. SEM images of (a) non-PM, and (b) PM fibers. (c) Left axis: GVD of the non-PM fiber (green) and the two fundamental modes of the PM fiber - mode I (red-dot), mode II (red-dash). Right axis: PM fiber group birefringence (blue-dot).

used for coupling and a half-wave plate (Thorlabs AQWP10M-1600) was used to control the polarization orientation.

The SC output was coupled into a 170 m long dispersion-shifted fiber (DSF) for shot-to-shot spectral measurements using DFT [14–16]. The input to the DSF was attenuated to ensure linear propagation. The DSF had normal GVD of $\beta_2 = 107 \text{ ps}^2/\text{km}$, and dispersion slope $\beta_3 = 0.082 \text{ ps}^3/\text{km}$ at $1.55 \mu\text{m}$. The DFT setup used a 50 GHz InGaAs detector (u2t: XPDV2120R) and a 12 GHz 40 GS/s oscilloscope (Agilent DSA91204A). The pulse train was recorded for $5 \mu\text{s}$, corresponding to 400 consecutive SC pulses. The 5.8 nm spectral resolution of the DFT was limited by the system bandwidth.

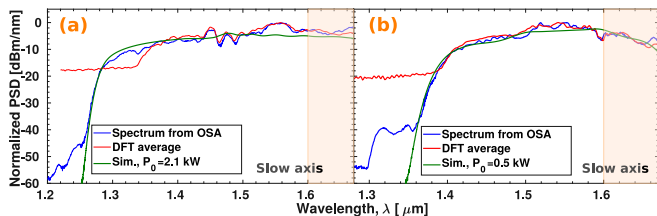


Fig. 2. Spectra measured using the OSA (blue), DFT average (red), and from simulations when light is coupled along the slow axes (green): (a) for the non-PM fiber using vector simulations with $P_0 = 2.1 \text{ kW}$; and (b) the PM fiber using scalar simulations with $P_0 = 0.5 \text{ kW}$.

Figures 2(a,b) show the average SC spectra measured using DFT (red) for $P_0 = 2.1 \text{ kW}$ for the non-PM fiber and $P_0 = 0.5 \text{ kW}$ for the PM fiber. Spectra measured using an optical spectrum analyzer (OSA) (Agilent 86142B) are plotted in blue, and the simulated SC spectrum in green (simulation details are given later). The DFT and OSA spectra agree well for wavelengths longer than $1.35 \mu\text{m}$ but there is poorer agreement at shorter wavelengths because of the effect of DSF dispersive terms higher than β_3 . However, this short wavelength mismatch does not affect the conclusions that can be drawn. We also note that the reduced sensitivity of the InGaAs detector and lower SC power above $1.6 \mu\text{m}$ results in unreliable RIN measurements.

Hence, we limit our discussion to wavelengths below $1.6 \mu\text{m}$, with longer wavelengths (the shaded region) shown only for reference.

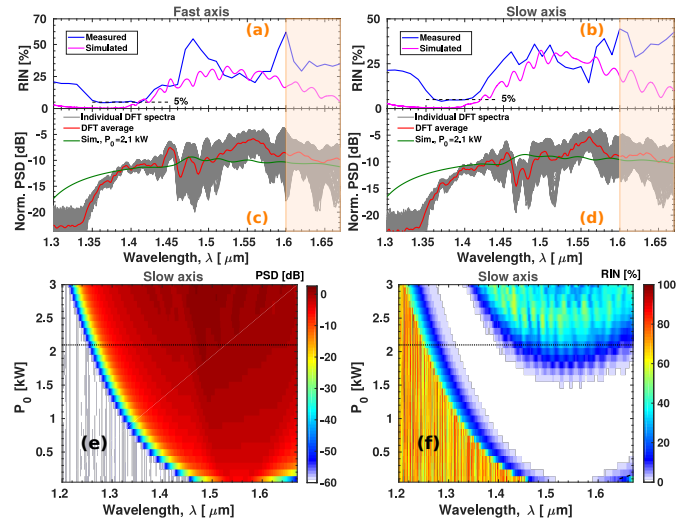


Fig. 3. Results for the non-PM ANDi fiber: Measured and simulated SC RIN when light was coupled into the fast axis (a), and when light was coupled into the slow axis (b). The measured 400 individual DFT spectra (gray) and the DFT average (red) and simulated SC for $P_0 = 2.1 \text{ kW}$ (green), when light was coupled into the fast axis (c), and when light was coupled into the slow axis (d). SC spectra from CGNLSE simulations with P_0 varied from 0.1 kW to 3 kW (40 power increments) when light was coupled into the slow axis (e) and the corresponding RIN plots (f).

Power was coupled into the fast axis of the non-PM ANDi fiber. The DFT average (red) is plotted in Fig. 3(c). The gray lines are the 400 individual DFT spectra. Relative intensity noise (RIN) was calculated as the ratio of standard deviation to mean of the 400 DFT spectra and is shown in Fig. 3(a). The input polarization into the non-PM ANDi fiber was then rotated by 90° in order to couple into the slow axis of the fiber. Fig. 3(d) shows the DFT average of the spectrum (red) and the 400 individual pulses (gray), and RIN of the SC is shown in Fig. 3(b). The two fundamental axes of the fiber were identified by observing the polarization of the light out of the fiber at a low power, while the input polarization to the fiber was varied. At the powers used in the experiments, the axis at which the broadest SC was generated is denoted as the fast axis, as the dispersion for the pump pulse when coupled to this axis is lower than the dispersion when coupled to the slow axis.

CGNLSE [17] was used to numerically simulate the SC and the noise properties of the SC in the non-PM ANDi fiber. The effective refractive index of the fiber was numerically calculated using the fiber parameters, and the full dispersion profile of the fiber is used in the simulations. The mode profile dispersion is included in the simulation such that the photon number is conserved when the net loss is zero [18]. The total loss of the fiber was included in the simulation and was calculated as the numerically obtained confinement loss and the fiber material loss measured in Ref. [13]. The weak birefringence between the two fundamental modes was accounted by their phase mismatch, $\Delta\beta = \Delta n \omega_0 / c$, where ω_0 is the angular frequency of the pump. The implementation of the CGNLSE is similar to that in Ref. [10].

Nonlinear index, $n_2 = 4.88 \times 10^{-19} \text{ m}^2\text{W}^{-1}$, birefringence, $\Delta n = 10^{-7}$, and the Raman response curve with single Lorentzian profile with damping time of vibrations, $\tau_1 = 5.5 \text{ fs}$, $\tau_2 = 32 \text{ fs}$, and fractional contribution of the delayed Raman response, $f_R = 0.2$ were used in the simulations. The input pulse was Gaussian with $T_{FWHM} = 225 \text{ fs}$. Quantum noise in the pump was included by adding independent and normally distributed real and imaginary parts in each time bin with width Δt of the input envelope function in the Wigner representation. The quantum noise has a variance of $\hbar\omega_0/2\Delta t$ [19, 20]. The pump was measured to have a RIN = 0.6%, using the DFT technique. This technical laser noise was added to the P_0 of the input pulse such that energy $P_0 T_{FWHM}$ was constant [7, 21]. All RIN calculations were carried out using an ensemble of 20 independent simulations with different noise seeds, and all simulated spectra plotted in the figures are averaged over 20 individual simulations.

The blue curve in Fig. 2(a) shows the SC recorded with the OSA for the non-PM fiber when coupled into the slow-axis, and the green curve is the spectrum from the CGNLSE simulation with $P_0 = 2.1 \text{ kW}$. The simulation reproduces the experimental data very well. The SC spectra of the 400 individual shots for the slow axis are plotted in Fig. 3(d), the average DFT spectrum is plotted in red, and the green curve is the spectra obtained from the CGNLSE simulations with $P_0 = 2.1 \text{ kW}$. The measured averaged DFT spectra (red) is plotted in Fig. 2(a), as well, for reference. Fig. 3(b) shows the corresponding RIN plot. The blue curve is the RIN characteristic calculated from the experimental DFT data and the magenta curve is the RIN calculated from the CGNLSE simulations. The RIN obtained from the DFT data exceeds 5% [marked with dashed line in Figs. 3(a,b)] over the whole SC width and at wavelengths longer than $1.4 \mu\text{m}$ reaches levels higher than 50% [when coupled to the slow axis, shown in Fig. 3(b)]. The amplitudes of DFT-measured shot-to-shot fluctuations match the RIN profile obtained from the simulations. Specifically, the simulation follows well the slope at wavelengths where the RIN begins to rise, at the shorter wavelength side. Similarly Fig. 3(c) shows the measured and simulated spectra for the fast axis and corresponding RIN curves are plotted in Fig. 3(a). Fig. 3(e) shows SC from forty sets of CGNLSE simulations with P_0 varied from 0.1 kW to 3 kW for the slow axis. The dotted horizontal line marks the spectrum generated with $P_0 = 2.1 \text{ kW}$, corresponding to the P_0 used in the experiment. The corresponding RIN plotted in Fig. 3(f) show that, an input P_0 greater than 1.5 kW results in large pulse-to-pulse fluctuations in the output SC. Plots in Fig. 3(a-f) show that, when a weakly-birefringent ANDi fiber is used along with a relatively long pump pulse and a large absolute value of dispersion, the SC generation dynamics exhibits large pulse-to-pulse fluctuations in most of the cases due to PMI, as shown in Ref. [10]. To verify the origin of the large pulse-to-pulse fluctuations observed in the non-PM fiber, we implemented a separate scalar-GNLSE simulation in the interaction picture [22] with all the input parameters same as in the CGNLSE simulations. The implementation of the scalar-GNLSE is similar to that in Ref. [7], and further details on the implementation can be there. We carried out forty sets of scalar-GNLSE simulations with P_0 varied from 0.1 kW to 3 kW for the non-PM fiber. The spectrum at the end of fiber is plotted in Fig. 4(a) and the corresponding RIN plots are shown in Fig. 4(b). The dotted horizontal lines in Figs. 4(a-b) mark the $P_0 = 2.1 \text{ kW}$ used in the experiments. The RIN plots in Fig. 4(b) show that pulse-to-pulse fluctuations in the SC as a result of mixed parametric Raman (MPR) noise alone is low for all the P_0 in the plot and therefore the high RIN observed in Fig. 3(f) is indeed from PMI.

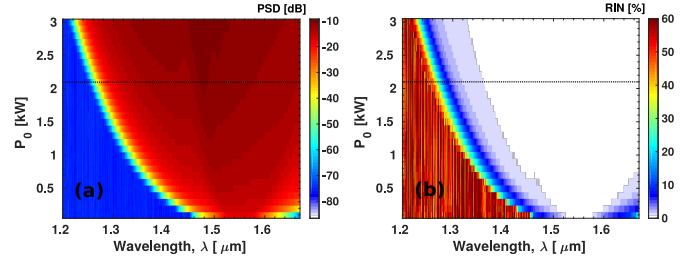


Fig. 4. Numerical results for the non-PM ANDi fiber: (a) Colormap of SC obtained using scalar-GNLSE simulations with increasing P_0 from 0.1 kW to 3 kW (set of forty simulations), and **(b)** the corresponding numerical RIN traces.

Next, we investigated the noise characteristics of the SC using the PM variant of the fiber. The pump polarization was first aligned to the fast axis of the PM ANDi fiber. The measured DFT average (red) is plotted in Fig. 5(c). The gray traces are the overlaying spectra of the 400 SC shots resolved using the DFT. The polarization of the pump was then rotated by 90° in order to couple into slow axis of the fiber. Fig. 5(d) shows the measured DFT average (red) and the 400 individual spectra (gray) in this case. RIN of the SC when coupled into the slow axis of the fiber is shown in Fig. 5(b). The SC and the RIN out of the fiber were simulated using scalar-GNLSE. The blue curve in Fig. 2(b) is the measured spectrum with the OSA and the green curve is the spectrum obtained from the scalar-GNLSE simulations for the slow axis with $P_0 = 0.5 \text{ kW}$. We see that the scalar-GNLSE simulation agrees very well with the measured spectra. All the 400 measured DFT spectra for the slow axis are plotted in Fig. 5(d), the average DFT spectra is plotted in red, and the green curve is the spectra obtained from the scalar-GNLSE simulations with $P_0 = 0.5 \text{ kW}$. The measured DFT average (red) is plotted in Fig. 2(b), as well, for reference. Fig. 5(b) shows the corresponding RIN plot. The blue curve is the experimental RIN calculated using the DFT spectra. The measured RIN is low and is around 1% [marked with dashed line in Figs. 5(a)] over the whole SC width where our DFT measurements are accurate. The magenta curve is the RIN numerically calculated from the simulations. The measured shot-to-shot fluctuations, characterized in terms of RIN, agrees very well with the RIN obtained from the simulations. Specifically, the simulation follows well the low-RIN measured in the experiments for wavelengths shorter than $1.6 \mu\text{m}$, where our measurements are accurate. Similarly, Fig. 5(c) shows the measured and simulated spectra for the fast axis and corresponding RIN curves are plotted in Fig. 5(a). Fig. 5(e) shows SC from forty sets of scalar-GNLSE simulations with P_0 varied from 0.1 kW to 3 kW for the slow axis. The dotted horizontal line marks the spectrum generated with $P_0 = 0.5 \text{ kW}$, corresponding to the P_0 used in the experiments. The corresponding RIN plots in Fig. 5(f) show that for all the peak powers used in the simulation the RIN of the SC out of the PM ANDi fibers remains extremely low.

The vector-GNLSE simulations for the non-PM fiber and the scalar-GNLSE simulations for the PM fiber are able to accurately reproduce the results obtained in the experiments. This allows us to confidently use the simulation to compare the noise properties of the two fibers. It is noted that even though the same configuration of the pump setup was used in the experiments with the PM fiber, the power coupled into the PM fiber was lower than that into the non-PM fiber. This is attributed to the

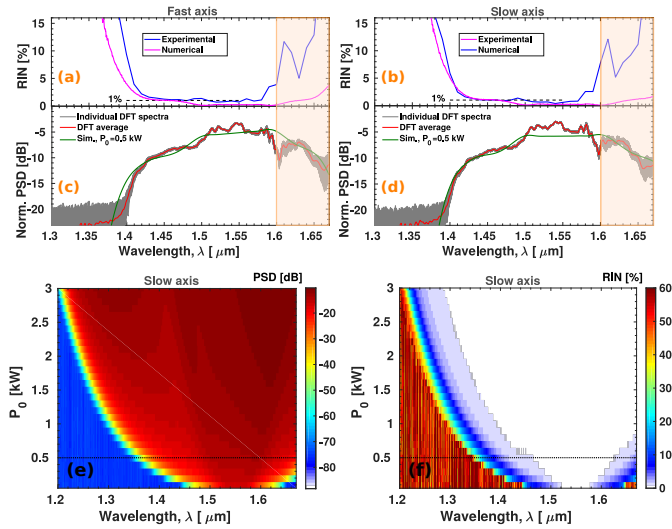


Fig. 5. Results for the PM ANDi fiber: Measured and simulated RIN of the SC out of the fiber when light was coupled into the fast axis (a), and when light was coupled into the slow axis (b). The measured 400 individual DFT spectra (gray) and the DFT average (red) and simulated SC for $P_0 = 0.5$ kW (green), when light was coupled into the fast axis (c), and when light was coupled into the slow axis (d). SC at the end of the fiber obtained using scalar GNLSE simulations with P_0 varied from 0.1 kW to 3 kW (forty set of simulations) when light was coupled into the slow axis (e), and the corresponding RIN plots (f).

presence of the large holes introduced to induce birefringence which leads to higher mode mismatch between the focused beam and the fundamental modes of this fiber. In spite of the difference in peak power coupled into the PM and non-PM fiber we can directly compare the noise properties of the two as all other parameters in the experiments were the same.

SC out of an all-solid soft glass, low-birefringent ANDi fiber, pumped by a 390 fs laser pulse at $1.55 \mu\text{m}$ was used in DFT noise study in Ref. [5]. Unlike in our case the noise observed was attributed to MPR noise and PMI was not associated with the observed pulse-to-pulse fluctuations. SC out of a germanium doped PM ANDi fiber, pumped by a 25 fs laser pulse at $1.55 \mu\text{m}$ was studied in Ref. [8]. Even though the individual DFT spectra seemed relatively stable, the pulse-to-pulse noise quantified as SNR (which is the inverse of RIN) shows large variation across the SC spectrum. These results individually do not provide a clear picture of the conditions needed to obtain a low-noise SC. Therefore, we have studied the noise properties of the SC for both the PM and the non-PM ANDi fibers and we have experimentally verified it in the relatively long fs pulse regime. It can be seen from the RIN plot for the SC from the non-PM fiber [Fig. 3(f)] that for a low pump peak power P_0 the RIN remains low but then it rises because of PMI as P_0 increases. However, for the same set of pulse duration's and the set of peak powers, the SC out of the PM fiber always remains low-noise [see Fig. 3(f)], when pumped along its fundamental axis.

In conclusion, we have experimentally characterized fluctuations in SC generation from a weakly-birefringent non-PM ANDi fiber and its PM version when pumped by 225 fs pulses at $1.55 \mu\text{m}$. The experimentally measured RIN was reproduced very well using CGNLSE simulations for the non-PM fiber, and using

scalar-GNLSE simulations for the PM fiber. We have shown that for the non-PM fiber PMI plays a detrimental role while attempting to maintain low-noise, and for the fiber and pump parameters used in our case, MPR noise has a negligible effect. Finally, using the same pump conditions, we have demonstrated that it is indeed possible to obtain ultra-low-noise ($\text{RIN} < 1\%$) SC when pumping along the fundamental axis of the PM version of the ANDi fiber.

Funding. Horizon 2020 Framework Programme Marie Curie grant No. (722380 [SUPUVIR]); Villum Fonden (2021 Vilum Investigator: Table-Top Synchrotrons); Fundacja na rzecz Nauki Polskiej (FNP) (First TEAM/2016-1/1 - POIR.04.04.00-00-1D64/16-00); Agence Nationale de la Recherche (ANR) (ANR-15-IDEX-0003, ANR-17-EURE-0002, ANR-21-ESRE-0040).

Disclosures. The authors declare no conflicts of interest.

Data availability. Data underlying the results may be obtained from the authors upon reasonable request.

REFERENCES

1. A. Rampur, D.-M. Spangenberg, B. Sierro, P. Hänzli, M. Klimczak, and A. M. Heidt, *Appl. Phys. Lett.* **118**, 240504 (2021).
2. S. Rao D. S., M. Jensen, L. Grüner-Nielsen, J. T. Olsen, P. Heiduschka, B. Kemper, J. Schnekenburger, M. Glud, M. Mogensen, N. M. Israelsen, and O. Bang, *Light. Sci. & Appl.* **10**, 1 (2021).
3. K. J. Kaltenecker, S. Rao D. S., M. Rasmussen, H. B. Lassen, E. J. R. Kelleher, E. Krauss, B. Hecht, N. A. Mortensen, L. Grüner-Nielsen, C. Markos, O. Bang, N. Stenger, and P. U. Jepsen, *APL Photonics* **6**, 066106 (2021).
4. T. Sylvestre, E. Genier, A. N. Ghosh, P. Bowen, G. Genty, J. Troles, A. Mussot, A. C. Peacock, M. Klimczak, A. M. Heidt, J. C. Travers, O. Bang, and J. M. Dudley, *J. Opt. Soc. Am. B* **38**, F90 (2021).
5. M. Klimczak, G. Soboń, R. Kasztelaniec, K. M. Abramski, and R. Buczyński, *Sci. Reports* **6**, 19284 (2016).
6. N. Nishizawa, T. Niinomi, Y. Nomura, L. Jin, and Y. Ozeki, *IEEE J. Sel. Top. Quantum Electron.* **24**, 1 (2018).
7. S. Rao D. S., R. D. Engelsholm, I. B. Gonzalo, B. Zhou, P. Bowen, P. M. Moselund, O. Bang, and M. Bache, *Opt. Lett.* **44**, 2216 (2019).
8. K. Tarnowski, T. Martynkien, P. Mergo, J. Sotor, and G. Soboń, *Sci. reports* **9**, 1 (2019).
9. A. M. Heidt, J. S. Feehan, J. H. V. Price, and T. Feurer, *J. Opt. Soc. Am. B* **34**, 764 (2017).
10. I. B. Gonzalo, R. D. Engelsholm, M. P. Sørensen, and O. Bang, *Sci. Reports* **8**, 6579 (2018).
11. A. M. Heidt, J. M. Hodasi, A. Rampur, D.-M. Spangenberg, M. Ryser, M. Klimczak, and T. Feurer, *Sci. reports* **10**, 1 (2020).
12. E. Genier, A. N. Ghosh, S. Bobba, P. Bowen, P. M. Moselund, O. Bang, J. M. Dudley, and T. Sylvestre, *Opt. Lett.* **45**, 3545 (2020).
13. M. Klimczak, D. Michalik, G. Stępniewski, T. Karpate, J. Cimek, X. Forestier, R. Kasztelaniec, D. Pysz, R. Stępień, and R. Buczyński, *J. Opt. Soc. Am. B* **36**, A112 (2019).
14. B. Wetzel, A. Stefani, L. Larger, P.-A. Lacourt, J.-M. Merolla, T. Sylvestre, A. Kudlinski, A. Mussot, G. Genty, F. Dias, and J. M. Dudley, *Sci. reports* **2**, 882 (2012).
15. T. Godin, B. Wetzel, T. Sylvestre, L. Larger, A. Kudlinski, A. Mussot, A. B. Salem, M. Zghal, G. Genty, F. Dias, and J. M. Dudley, *Opt. Express* **21**, 18452 (2013).
16. K. Goda and B. Jalali, *Nat. Photonics* **7**, 102 (2013).
17. G. P. Agrawal, *Nonlinear Fiber Optics* (Academic Press, 2012), 5th ed.
18. J. Lægsgaard, *Opt. Express* **15**, 16110 (2007).
19. J. F. Corney and P. D. Drummond, *J. Opt. Soc. Am. B* **18**, 153 (2001).
20. B. Zhou and M. Bache, *APL Photonics* **1**, 050802 (2016).
21. E. Genier, P. Bowen, T. Sylvestre, J. M. Dudley, P. Moselund, and O. Bang, *J. Opt. Soc. Am. B* **36**, A161 (2019).
22. J. Hult, *J. Light. Technol.* **25**, 3770 (2007).